Optimization of thermoelectric performance for heterogeneous $Ca_{0.9}R_{0.1}MnO_3$ (R=Dy, Yb) ceramics

Teng Wang[a], Hongchao Wang[a], Wenbin Su[a], Jinze Zhai[a], Xue Wang[a], Yazhou Ran[a], Tingting Chen[a], Chunlei Wang[a]

[a] *School of Physics, State Key Laboratory of Crystal Materials, Shandong University, Jinan 250100, China*

Hongchao Wang wanghc@sdu.edu.cn

Chunlei Wang wangcl@sdu.edu.cn

Abstract

Perovskite manganite Ca0.9R0.1MnO3-δ (R=Dy, Yb) ceramics have been synthesized by traditional solid-state reaction with multi-calcination processes. A heterogeneous microstructure including large and small micrometer-sized grains, coherent interfaces and oxygen defects have been formed with optimized calcination time. The carrier concentration of the third-calcined samples is enhanced approximately 3 times compared with those synthesized through conventional methods. Thus, the electrical resistivity of the third-calcined $Ca_{0.9}R_{0.1}MnO_{3-\delta}$ (R=Dy, Yb) ceramic samples obviously decreases, leading to higher power factor. Additionally, the thermal conductivity is also reduced by multi scale scattering of heterogeneous structure. The lowest lattice thermal conductivities of Dy or Yb doped samples are 1.24 $Wm^{-1}K^{-1}$, 1.22 $Wm^{-1}K^{-1}$ respectively. Thus, high thermoelectric

performance for $Ca_{0.9}R_{0.1}MnO_{3-\delta}$ (R=Dy, Yb) has been achieved by the multi-calcination process. The highest figure of merit is almost 30% higher than that of the first-calcined samples. Therefore, a heterogeneous microstructure formed by optimized multi-calcination can effectively optimize the thermoelectric performance of oxides.

1. Introduction

Thermoelectric materials, which can convert waste heat into electricity directly, are playing an important role in sustainable energy [1-3]. Their potential for thermoelectric practical applications is determined by the dimensionless figure of merit, which is defined as $zT = S^2T/\rho\kappa$, where S is the Seebeck coefficient, ρ the electrical resistivity, κ the total thermal conductivity, and T the absolute temperature in Kelvin[4-5]. In this expression, S^2/ρ is the power factor (PF) and is related to the electric properties. To maximize the zT of a material, a large S, low ρ and low κ are needed. However, these three parameters are inter-correlated, which makes difficult to separately control them to produce a high thermoelectric performance in one material[3]. Therefore, many techniques, such as doping, band engineering, and nanostructuring, have been tried to achieve a high zT, and several high figures of merit have been found in some thermoelectric materials[6-9].

Metal oxides, due to their high thermal and chemical stability, oxidation resistance, and low cost, have been promising thermoelectric materials[10]. This promise has increased with the discovery of p-type $NaCo_2O_4$[11], which possesses excellent

thermoelectric performance and is comparable to several traditional alloys. Hence, metal oxides as thermoelectric materials have attracted considerable attention. In many researched thermoelectric oxides, their layered structure shows excellent thermoelectric performance and can be optimized by doping, nanostructuring and so on[12-15]. Through dual doping with Ag and Lu, the microstructures of $Ca_3Co_4O_9$-based ceramics show metallic nanoinclusions of Ag, and thus the figure of merit is improved to zT~0.61[14]. By heavily doping with Ba and refining grain sizes, the layered BiCuSeO system presents a high figure of merit of 1.1 at 923 K[15]. Additionally, the figure of merit for flaky single crystal $Na_xCoO_{2-\delta}$, prepared by a flux technique, can exceed 1.0 because of its high power factor[11]. As per the above description, several high figures of merit have been achieved in some layered thermoelectric oxides, with p-type semiconducting behaviour. In thermoelectric devices applications, high thermoelectric performance of n-type oxides is required and should be comparable to p-type performance[6]. Therefore, the thermoelectric performance of n-type oxides has attracted more attention and many studies have been conducted. To date, the thermoelectric performance of n-type thermoelectric oxides have not broken through, and the figures of merit are approximately 0.1-0.4, which are inferior to well-studied p-type thermoelectric oxides. Therefore, thermoelectric performance of n-type thermoelectric oxides should be further improved for applications with matched p-type oxides. $CaMnO_3$ (CMO) is a typical n-type thermoelectric oxide that may achieve high thermoelectric performance in the future through optimization. In the past few years, elemental doping has been utilized as the main method to improve the

figure of merit of CMO oxides, and large relative studies have been performed. Generally, depending on the sites where dopants are substituted, there are two types of single doping. One type is single-element doping at Mn site[16], and the other type is doping at Ca site. Compared with substitution at Mn site, doping elements at Ca site more easily achieve high thermoelectric performance[6]. Dopants such as Bi, Y, La, Ce, Dy, Nd, Tb, Ho, Yb, and Lu with tri- or tetravalent oxidation state can increase the carrier concentration[17-19]. The increase in carrier concentration leads to a marked decrease in the electrical resistivity and a moderate decrease in the Seebeck coefficient, leading to good thermoelectric performance. Among all these doping elements, Dy and Yb elements are good candidate dopants for CMO at an optimized doping amount of approximately 10%. Overall, elemental doping can improve the figure of merit of CMO to certain degree, and the effect of Dy or Yb dopants on thermoelectric performance is especially significant.

Generally, the use of synthesis technology is important to optimize physical transport in thermoelectric materials. Different quenching media can result in different microstructures and thus affect thermoelectric performance. Heterogeneous PbTe nanocomposites are synthesized by quenching into ice water. Their figure of merit can be enhanced by 25% compared with homogenous samples[20]. By applying a hot-forging process to produce textured microstructures, $Bi_{0.875}Ba_{0.125}CuSeO$ reaches a record zT of 1.4 at 923 K[21]. As in hot-forged $Bi_{0.5}Sb_{1.5}Te_3$ alloys, in situ nanostructures and high-density lattice defects were observed, which led to a higher power factor, lower thermal conductivity and, ultimately, a peak zT value of 1.3[22]. Moreover, reduced

$SrTiO_3$ ceramics prepared by controlling the heating rate of plasma sintering, have reached an impressive *zT* value of 0.4 at 823 K[23]. This figure of merit is the highest determined so far for bulk $SrTiO_3$ ceramics. In summary, the optimization of synthesis conditions can effectively enhance thermoelectric performance.

In here, heterogeneous $Ca_{0.9}R_{0.1}MnO_3$ (CMO:R) (R=Dy, Yb) samples have been prepared by a multi-calcination process, and their relative thermoelectric performance was evaluated. The carrier concentration and mobility have been simultaneously improved by the third calcination. These improvements led to a lower electrical resistivity and a higher power factor. Thermal conductivity is reduced by multi-scattering through heterogeneous microstructure, leading to the highest figures of merit, *zT*=0.12 and 0.14, in the third-calcined CMO:R (R=Dy, Yb) samples, respectively.

2. Experimental Details

$Ca_{0.9}R_{0.1}MnO_3$ (R=Dy, Yb) ceramics were synthesized by solid state reaction with a multi-calcination process. The starting materials were $CaCO_3$ (99%), MnO_2 (97.5%), Dy_2O_3 (99.99%), and Yb_2O_3 (99.99%). After the raw materials were weighed in stoichiometric proportions, they were mixed by ball milling in ethanol with zirconia balls for 12 h. Then, the mixtures were dried, cold pressed into pellets and calcined at different times in air with intermediate grinding. The samples were assigned as CMO:R-1, -2, -3, -4, (R=Dy, Yb) for different calcined times. The detailed calcination processes are as follows: CMO:R-1: the cold-pressed pellets were

calcined at 1373 K for 4 h in air. CMO:R-2: the cold-pressed pellets were calcined at 1073 K for 4 h in air and then reground by hand, pressed into pellets, and calcined a second time at 1373 K for 4 h in air. For CMO:R-3 and CMO:R-4, the calcination process was similar to CMO:R-2 and only differed in the calcined temperature settings. For CMO:R-3, the calcined temperature settings were 1073 K/4 h, 1173 K/4 h and then 1373 K/4 h. For CMO:R-4, the temperature settings were 1073 K/4 h, 1173 K/4 h, 1273 K/4 h and 1373 K/4 h, sequentially performed. After multi-calcination, the pellets were reground and then ball milled for 12 h to obtain fine powders, which were pressed into pellets and sintered at 1523 K for 4 h in air and then naturally cooled to room temperature in the furnace to produce the final samples.

The structure of all samples was studied using a Bruker AXS D8 ADVANCE diffractometer with Cu Kα radiation at room temperature. The surface morphology and energy dispersive spectroscopy (EDS) mapping were obtained on a JSM-6701F scanning electronic microscope (SEM). Transmission electron microscopy (TEM) was carried out using a JEM-2100F microscope. Specimens for TEM were prepared by a focused ion beam (FIB). The Hall resistivity was measured with a home-made Hall system using a four-probe structure under magnetic fields of ±0.6 T. The carrier concentration was calculated based on $n=1/eR_H$, where e is the electronic charge and R_H is the Hall coefficient, while carrier mobility was calculated using $\mu=1/\rho R_H$, where ρ is the electric resistivity. The electrical resistivity and Seebeck coefficient were measured in the temperature range between 300 K and 1100 K with a LINSEIS LSR-3 equipment. The thermal diffusivity values (λ) were measured by a laser flash

apparatus NETZSCH LFA-457 directly from room temperature to 1073 K. The thermal conductivity (κ) was calculated by the formula $\kappa=\lambda C_p d$, where C_p is the heat capacity. Here, the C_p of CMO:Dy is an average value of all Dy-doped samples. Similarly, the C_p of CMO:Yb is also the average value of all Yb-doped samples. The C_p for each sample was derived using standard samples (Pyroceram) in LFA457. Furthermore, d is the density of the sample, which was measured by the Archimedes' method. The power factor and zT were calculated from the above measured parameters.

3. Results and Discussion

The room temperature XRD patterns of the multi-calcined CMO:R (R=Dy, Yb) samples are shown in **Figure 1**. Although the CMO:R (R=Dy, Yb) samples were synthesized with different calcined times, all samples exhibit an orthorhombic perovskite structure and no secondary phase peak is observed. The lattice parameters and theoretical densities for all samples are calculated and shown in **Table S1**. The values of CMO:R-1 (R=Dy, Yb) are consistent with reported values of $Ca_{0.9}Dy_{0.1}MnO_3$ and $Ca_{0.9}Yb_{0.1}MnO_3$ in previous studies[24]. Moreover, a slight and irregular fluctuation in lattice parameters was observed with the multi-calcinations of the CMO:R (R=Dy, Yb) samples. This result may be attributed to the valence variation of Mn and the exact oxygen content, which may be affected by the multi-calcinations. The relative densities are calculated based on experimental and theoretical densities. The relative density values for the CMO:Dy samples are the

same, specifically, 92%. In the CMO:Yb samples, the relative density values range from 91%-94% with slight variations. Therefore, high-density samples of CMO:R (R=Dy, Yb) have been synthesized.

The temperature dependence of the electrical resistivity (ρ) of CMO:R (R=Dy, Yb) from 300 K to 1100 K is shown in **Figures 2(a) and 3(a)**. The Dy- and Yb-doped samples are all semiconductors and show metallic-like behavior as ρ increases with increasing temperature in the entire measured temperature range. In addition, the values of electrical resistivity of the multi-calcined samples are much lower than those of undoped CMO due to the increased carrier concentration that results from the substitution of R^{3+} for Ca^{2+}[17, 25]. Furthermore, multi-calcination process leads to heterogeneous microstructure of multi-calcined samples, as it will be discussed and shown in **Figures 8** and **9**, including many coherent interfaces from the phase dispersion. These may result to increase of the carrier concentration, and the effect of multi-calcination process may be similar with one more dopant. Thus, the electrical resistivity of multi-calcined CMO:R (R=Dy, Yb) is comparable with some dual-doped CMO samples[25]. It is clear that the third-calcined samples present the lowest electrical resistivity for CMO:R (R=Dy, Yb), being 3.98 mΩ • cm at 326 K for CMO:Dy and 3.29 mΩ • cm for CMO:Yb at 476 K. These values are attributed to the high carrier concentration and mobility for the third-calcined CMO:R (R=Dy, Yb) samples, as shown later in **Figure 6**. With the same chemical composition of CMO:Dy or CMO:Yb, the carrier concentration and mobility are significantly affected by multi-grinding and multi-calcination. Thus, the heterogeneous microstructure, as it

will be observed in **Figures 7** and **8**, formed during multi-fabrication processes can effectively affect the carrier concentration and mobility and then modify the electrical resistivity of CMO:R (R=Dy, Yb) compositions.

Figure 2(b) presents the Seebeck coefficient for multi-calcined CMO:Dy. The Seebeck coefficients for all samples are negative, which indicates that electrons are the dominant carriers. This is consistent with the negative value of the carrier concentration, as it will be discussed and shown in **Figure 6**. With an increase in temperature, the absolute values of the Seebeck coefficients are increased, which is a typical degenerate semiconductor behavior, in agreement with previous work[9]. However, the absolute values of the Seebeck coefficients are slightly decreased for multi-calcined samples at high temperatures, probably resulting from the bipolar effect at high temperature[10]. Although the samples are multi-grounded and multi-calcined during the synthesis process, the Seebeck coefficients for all samples are not obviously changed in the entire measured temperature range. Thus, the Seebeck coefficient for CMO:Dy composition cannot be significantly affected by various synthesis technologies and maintains the high Seebeck coefficient for CMO. In the multi-calcined CMO:Yb samples, the behavior of Seebeck coefficient vs temperature is the same determined in CMO:Dy, as shown in **Figure 3(b)**. Overall, the multi-calcination synthesis process cannot significantly affect the Seebeck coefficient for CMO:R (R=Dy, Yb) and will maintain a high value while the carrier concentration is changed with multi-calcination.

From the measured values of electrical resistivity and Seebeck coefficient, the

power factor (*PF*) values of CMO:R (R=Dy, Yb) have been calculated using S^2/ρ, and shown in **Figures 2(c)** and **3(c**). The power factor for all samples are increased up to, approximately, 700 K and then decreased with a further increase in temperature. Evidently, the third-calcined CMO:R (R=Dy, Yb) samples obtain the highest power factor, 240 $\mu WK^{-2}m^{-1}$ for CMO:Dy at 676 K, and 339 $\mu WK^{-2}m^{-1}$ for CMO:Yb at 678 K. These values are larger than that of the first calcined sample, which suggest that these samples are better than conventionally synthesized samples. This enhancement of power factor is attributed to the low electrical resistivity and high Seebeck coefficient achieved by the multi-calcination in the above description.

The temperature dependence of the total thermal conductivity κ (closed symbols) and lattice thermal conductivity κ_L (open symbols) for CMO:R (R=Dy, Yb) are shown in **Figures 2(d)** and **3(d)**. The lattice thermal conductivity, κ_L, is obtained by subtracting the electronic thermal conductivity (κ_e) from the total thermal conductivity, κ. The electronic thermal conductivity, κ_e, is calculated using Wiedemann-Franz's law as $\kappa_e=LT/\rho$, where the Lorentz constant $L=2.44\times10^{-8}$ $W\Omega K^{-1}$. From a comparison with the values of the total thermal conductivity and lattice thermal conductivity, the last one is, approximately, 80% of the total thermal conductivity. Therefore, the lattice thermal conductivity is the main part of the thermal transport behavior, which is similar to previous works[25-26]. In the whole measured temperature range, the total and lattice thermal conductivities firstly decrease with temperature, and then increase, in all cases. The lowest total thermal conductivities are 1.49 $Wm^{-1}K^{-1}$ and 1.65 $Wm^{-1}K^{-1}$, and, the lowest lattice thermal conductivity values are 1.25 $Wm^{-1}K^{-1}$ and 1.33

$Wm^{-1}K^{-1}$ for the third-calcined CMO:Dy and CMO:Yb samples, respectively, at 672 K. These values are nearly 25% lower than that of first-calcined samples. Furthermore, these total thermal conductivities for our multi-calcined samples are almost the same compared with Dy&Yb dual-doped CMO sample (about 1.47 $Wm^{-1}K^{-1}$)[25]. Thus, the third-calcined CMO:R (R=Dy, Yb) samples present the lowest total and lattice thermal conductivity in all samples, which are strongly related to heterogeneous microstructures by multi-calcination, as previously mentioned and will be discussed in next sections. Overall, the thermal conductivity can be effectively optimized and it is easy to obtain lower values by the multi-calcination process.

The temperature dependence of the figure of merit, *zT*, for all samples is shown in **Figure 4**. In **Figure 4(a)**, the *zT* values of the multi-calcined CMO:Dy samples first increase to a maximum and then slightly decrease until the end of the measured temperature range. The highest figure of merit, *zT*=0.12, is obtained at 670 K, which is enhanced 33% comparing with first-calcined CMO:Dy. The figures of merit for the CMO:Yb samples increase with increasing temperature and then reach a stable value after approximately 670 K, as shown in **Figure 4(b)**. Therefore, the maximum of figure of merit, *zT*=0.14, is achieved at 670 K. This highest value is 27% higher than that of the first calcined CMO:Yb samples.

The maximum value of the figure of merit of each time calcined CMO:R (R=Dy, Yb) sample has been plotted in **Figure 5(a)**. The results indicate that the third-calcined samples show the highest figure of merit in all multi-calcined samples for both Dy- and Yb-doped CMO. To understand the contribution of the power factor

and thermal conductivity for the high figure of merit at the third-calcined sample, the percentage variations in the power factor, thermal conductivity and *zT*, normalized to CMO:R-1(R=Dy, Yb), are shown in **Figure 5(b)**. The power factor of the third-calcined CMO:Dy-3 sample is increased by 10.6%, and the thermal conductivity is decreased by 1.9%. Thus, the high figure of merit of the third-calcined CMO:Dy-3 sample is mainly from the increase in power factor. Moreover, in the third-calcined CMO:Yb sample, the power factor is increased by 2.6%, but the thermal conductivity is obviously decreased by 17.4%. Hence, the decrease of thermal conductivity is the main factor that contributes to the higher *zT*. Therefore, the high figures of merit of the multi-calcined CMO:R (R=Dy, Yb) samples are obtained at the third calcination process, and the main contributions to these values are different.

To understand the thermoelectric transport properties of the multi-calcined samples, the microstructures, carrier concentrations and mobilities have been presented as followed. **Figure 6** shows the SEM images of surface sections of the first- and third-calcined CMO:R (R=Dy, Yb) samples. These images indicate that the first-calcined CMO:R (R=Dy, Yb) samples large and small micrometer-sized grains, especially CMO:Yb-1. After the third calcination, the small-sized grains disappeared, which may have been dissolved in neighborhood grains and formed little larger micro-grains. This behavior can be explained through Ostwald ripening[27]. The molecules on the surface of the small particles are more energetic and thus less stable than the inner ones unless they dissolve into the grain. This change is consistent with one reported study regarding $SrTiO_3$ ceramics[23]. Although the small micro-grains

disappeared and formed larger grains after the third calcination, as shown in **Figure 6**, the grain sizes of the third-calcined samples are not much larger, and show different micro-grain distributions. Thus, this kind of microstructure with relative large micro-gain sizes may be better to optimize the carrier mobility and lattice thermal conductivity simultaneously. As an example, the EDS mapping and TEM images for multi-calcined CMO:Yb samples are also presented in **Figures 7** and **8**. For the first-calcined CMO:Yb samples, the Mn and Ca distribution is homogenous, it is hard to see the element-rich part in EDS mapping. The Yb distribution shows only slight differences. However, the heterogeneous distribution of Yb and Ca is clearly seen in the third-calcined CMO:Yb samples, which resulted from the multi-grinding and multi-calcination. To further confirm the heterogeneous distribution, the TEM specimen has been extracted from the micro-grain, not from the grain boundary by FIB, and the images are shown in **Figure 8**. Although the XRD pattern at room temperature for third-calcined CMO:Yb sample presents pure phase structure (see **Figure1**), the phenomenon of phase dispersion is evidently seen in high-, medium-magnification TEM image and HRTEM image. This may be relative with the resolution limit of XRD and is similar with previous reports[28]. Nevertheless, the first-calcined samples show a perfect HRTEM picture, and it is difficult to find the phase dispersion and defects. This phase dispersion for the third-calcined CMO:Yb sample is strongly related with the element distribution, shown in **Figure 7**. However, the exact composition of dispersed phase is not exactly clear and will be confirmed in future works. Additionally, the phase dispersion can form more coherence interfaces,

which is beneficial to optimize the lattice thermal conductivity and carrier mobility simultaneously[29]. Thus, the heterogeneous microstructure of multi-calcined samples has been formed, including large and small micrometer-sized grains, and coherence interfaces caused by phase dispersion.

Figure 9(a) shows the room temperature carrier concentration for multi-calcined CMO:R (R=Dy, Yb) samples. The carrier concentrations of the first calcined CMO:Dy and CMO:Yb samples are 2.70×10^{19} cm^{-3} and 2.06×10^{19} cm^{-3}, respectively, which are both consistent with previously reported data[26]. The carrier concentration of the CMO:R (R=Dy, Yb) samples with multi-calcination is increased, especially for the third-calcined samples. This may be attributed to the interfacial effect of more coherent interfaces from the phase dispersion in the third calcination process. The effect of these interfaces on the carrier concentration has been found in previous reports[30-31]. In addition, the microstructure of Bi_2Te_3 alloys has been modified by the hot forging as a new synthesis technology in previous work[32], and then the carrier concentration has been optimized. The carrier mobility at room temperature is shown in **Figure 9(b)**. The carrier mobility for all multi-calcined samples was not significantly changed, except for the third-calcined samples. This increase of carrier mobility may be related to the microstructure. With the multi calcination process, the micro-sized grains are slightly grown, as observed in **Figure 6**. This will reduce the carrier scattering and then enhance the carrier mobility. Additionally, the interfacial effect from phase dispersion can also optimize the carrier mobility. In the end, the multi-calcination process as alternative synthesis method can

form a heterogeneous microstructure to optimize the carrier concentration and mobility in CMO:R (R=Dy, Yb) samples, and then significantly decrease the electrical resistivity, as shown in **Figures 2** and **3**.

Regarding the lowest lattice thermal conductivity, achieved in the third-calcined CMO:R (R=Dy, Yb) samples, it also resulted from their heterogeneous microstructure. The different micro-sized grains can ensure the scattering of low-frequency phonons. Additionally, more coherent interfaces are formed by the phase dispersion, as shown in **Figure 8**, in the third-calcined sample after more hand regrinding and calcination. The more coherent interfaces can increase middle- and high-frequency phonon scattering and then reduce the lattice thermal conductivity. To date, the effect of coherent interfaces on lattice thermal conductivity has been confirmed in many thermoelectric alloys in previous investigations and has become an effective way to improve thermoelectric performance[33]. Therefore, heterogeneous microstructure including large and small micrometer-sized grains, and coherence interfaces, formed by multi-calcination can effectively scatter the low-, middle- and high-frequency phonons and obviously reduce the lattice thermal conductivity. Consequently, the heterogeneous microstructures can optimize the electrical properties and thermal conductivity simultaneously, and then enhance the thermoelectric figure of merit for CMO:R (R=Dy, Yb) samples.

4. Conclusions

Dy and Yb single-doped $CaMnO_3$ have been synthesized using a

multi-calcination method. A heterogeneous microstructure including large and small micrometer-sized grains, and coherence interfaces has been formed after multi-regrinding and multi-calcination. The carrier concentration and carrier mobility are simultaneously optimized in these heterogeneous microstructures, improving power factor. At the same time, the heterogeneous microstructure effectively scatters the low-, middle- and high-frequency phonons, leading to lower lattice thermal conductivity. Therefore, the electrical performance and thermal conductivity are all optimized, and the thermoelectric performance is enhanced. The figure of merit for the third-calcined CMO:Dy samples reach 0.12, which is 33% higher than the first-calcined ones, whereas the highest figure of merit, zT=0.14, is achieved for the third-calcined CMO:Yb samples, which is 27% enhanced compared with the first-calcined ones. As a consequence, the multi-calcination process can be seen as a better way to form heterogeneous microstructures which improve the thermoelectric performance of CMO oxides.

Acknowledgments

The work is financially supported by the National Basic Research Program of China of 2013CB632506, the Natural Science Fund of China under grant Nos. 51501105, 51672159, 51611540342, the Young Scholars Program of Shandong University under grant No. 2015WLJH21, the China Postdoctoral Science Foundation under grant Nos. 2015M580588 and 2016T90631, the Postdoctoral Innovation Foundation of Shandong Province under grant No. 201603027, the Fundamental

Research Funds of Shandong University under grant No. 2015TB019, and the Foundation of the State Key Laboratory of Metastable Materials Science and Technology under grant No.201703.

References

(1) Chu, S.; Cui, Y.; Liu, N. The path towards sustainable energy. *Nature materials* **2017,** *16* (1), 16-22.

(2) Sorrell, S. Reducing energy demand: A review of issues, challenges and approaches. *Renewable and Sustainable Energy Reviews* **2015,** *47*, 74-82.

(3) Snyder, G. J.; Toberer, E. S. Complex thermoelectric materials. *Nature materials* **2008,** *7* (2), 105-114.

(4) Bell, L. E. Cooling, heating, generating power, and recovering waste heat with thermoelectric systems. *Science* **2008,** *321* (5895), 1457-1461.

(5) Wood, C. Materials for thermoelectric energy conversion. *Reports on progress in physics* **1988,** *51* (4), 459-539.

(6) Wang, H.; Su, W.; Liu, J.; Wang, C. Recent development of n-type perovskite thermoelectrics. *Journal of Materiomics* **2016,** *2* (3), 225-236.

(7) Zhu, T.; Liu, Y.; Fu, C.; Heremans, J. P.; Snyder, J. G.; Zhao, X. Compromise and Synergy in High−Efficiency Thermoelectric Materials. *Advanced materials* **2017,** *29* (30), 1605884 (1-26).

(8) Wang, H.; Hwang, J.; Zhang, C.; Wang, T.; Su, W.; Kim, H.; Kim, J.; Zhai, J.; Wang, X.; Park, H. Enhancement of the thermoelectric performances of bulk SnTe alloys via

the synergistic effect of band structure modification and chemical bond softening. *Journal of Materials Chemistry A* **2017,** *5*, 14165-14173.

(9) Wang, H.; Wang, C. Synthesis of Dy doped $Yb_{0.1}Ca_{0.9}MnO_3$ ceramics with a high relative density and their thermoelectric properties. *Materials Research Bulletin* **2012,** *47* (9), 2252-2256.

(10) He, J.; Liu, Y.; Funahashi, R. Oxide thermoelectrics: The challenges, progress, and outlook. *Journal of Materials Research* **2011,** *26* (15), 1762-1772.

(11) Terasaki, I.; Sasago, Y.; Uchinokura, K. Large thermoelectric power in $NaCo_2O_4$ single crystals. *Physical Review B* **1997,** *56* (20), R12685.

(12) Sotelo, A.; Constantinescu, G.; Rasekh, S.; Torres, M.; Diez, J.; Madre, M. Improvement of thermoelectric properties of $Ca_3Co_4O_9$ using soft chemistry synthetic methods. *Journal of the European Ceramic Society* **2012,** *32* (10), 2415-2422.

(13) Sotelo, A.; Rasekh, S.; Madre, M.; Guilmeau, E.; Marinel, S.; Diez, J. Solution-based synthesis routes to thermoelectric $Bi_2Ca_2Co_{1.7}O_x$. *Journal of the European Ceramic Society* **2011,** *31* (9), 1763-1769.

(14) Van Nong, N.; Pryds, N.; Linderoth, S.; Ohtaki, M. Enhancement of the thermoelectric performance of p−type layered oxide $Ca_3Co_4O_{9+\delta}$ through heavy doping and metallic nanoinclusions. *Advanced materials* **2011,** *23* (21), 2484-2490.

(15) Li, J.; Sui, J.; Pei, Y.; Barreteau, C.; Berardan, D.; Dragoe, N.; Cai, W.; He, J.; Zhao, L. A high thermoelectric figure of merit zT> 1 in Ba heavily doped BiCuSeO oxyselenides. *Energy & Environmental Science* **2012,** *5* (9), 8543-8547.

(16) Bocher, L.; Aguirre, M.; Logvinovich, D.; Shkabko, A.; Robert, R.; Trottmann, M.;

Weidenkaff, A. $CaMn_{1-x}Nb_x O_3$ ($x \leq 0.08$) perovskite-type phases as promising new high-temperature n-type thermoelectric materials. *Inorganic chemistry* **2008,** *47* (18), 8077-8085.

(17) Ohtaki, M.; Koga, H.; Tokunaga, T.; Eguchi, K.; Arai, H. Electrical transport properties and high-temperature thermoelectric performance of $(Ca_{0.9}M_{0.1})MnO_3$ (M= Y, La, Ce, Sm, In, Sn, Sb, Pb, Bi). *Journal of Solid State Chemistry* **1995,** *120* (1), 105-111.

(18) Kobayashi, T.; Takizawa, H.; Endo, T.; Sato, T.; Shimada, M.; Taguchi, H.; Nagao, M. Metal-insulator transition and thermoelectric properties in the system $(R_{1-x}Ca_x)MnO_{3-\delta}$ (R: Tb, Ho, Y). *Journal of solid state chemistry* **1991,** *92* (1), 116-129.

(19) Wang, Y.; Sui, Y.; Fan, H.; Wang, X.; Su, Y.; Su, W.; Liu, X. High temperature thermoelectric response of electron-doped $CaMnO_3$. *Chemistry of Materials* **2009,** *21* (19), 4653-4660.

(20) Wang, H.; Hwang, J.; Snedaker, M. L.; Kim, I.-h.; Kang, C.; Kim, J.; Stucky, G. D.; Bowers, J.; Kim, W. High thermoelectric performance of a heterogeneous PbTe nanocomposite. *Chemistry of Materials* **2015,** *27* (3), 944-949.

(21) Sui, J.; Li, J.; He, J.; Pei, Y. L.; Berardan, D.; Wu, H.; Dragoe, N.; Cai, W.; Zhao, L. D. Texturation boosts the thermoelectric performance of BiCuSeO oxyselenides. *Energy & Environmental Science* **2013,** *6* (10), 2916-2920.

(22) Shen, J.; Zhu, T.; Zhao, X.; Zhang, S.; Yang, S.; Yin, Z. Recrystallization induced in situ nanostructures in bulk bismuth antimony tellurides: a simple top down route and

improved thermoelectric properties. *Energy & Environmental Science* **2010,** *3* (10), 1519-1523.

(23) Mehdizadeh Dehkordi, A.; Bhattacharya, S.; Darroudi, T.; Graff, J. W.; Schwingenschlögl, U.; Alshareef, H. N.; Tritt, T. M. Large thermoelectric power factor in Pr-doped $SrTiO_{3-\delta}$ ceramics via grain-boundary-induced mobility enhancement. *Chemistry of Materials* **2014,** *26* (7), 2478-2485.

(24) Park, J.; Kwak, D.; Yoon, S.; Choi, S. Thermoelectric properties of Bi, Nb co-substituted $CaMnO_3$ at high temperature. *Journal of Alloys and Compounds* **2009,** *487* (1), 550-555.

(25) Zhu, Y.; Wang, C.; Su, W.; Liu, J.; Li, J.; Zhang, X.; Mei, L. Influence of rare-earth elements doping on thermoelectric properties of $Ca_{0.98}$ $Dy_{0.02}MnO_3$ at high temperature. *Journal of Solid State Chemistry* **2015,** *225*, 105-109.

(26) Zhang, F.; Lu, Q.; Zhang, X.; Zhang, J. Preparation and improved electrical performance of the Pr-doped $CaMnO_{3-\delta}$ thermoelectric compound. *Physica Scripta* **2013,** *88* (3), 035705.

(27) De Smet, Y.; Deriemaeker, L.; Finsy, R. Ostwald ripening of alkane emulsions in the presence of surfactant micelles. *Langmuir* **1999,** *15* (20), 6745-6754.

(28) Wang, H.; Bahk, J. H.; Kang, C.; Hwang, J.; Kim, K.; Kim, J.; Burke, P.; Bowers, J. E.; Gossard, A. C.; Shakouri, A. Right sizes of nano-and microstructures for high-performance and rigid bulk thermoelectrics. *Proceedings of the National Academy of Sciences* **2014,** *111* (30), 10949-10954.

(29) Medlin, D.; Snyder, G. Interfaces in bulk thermoelectric materials: a review for

current opinion in colloid and interface science. *Current Opinion in Colloid & Interface Science* **2009,** *14* (4), 226-235.

(30) Ohta, H.; Kim, S.; Mune, Y.; Mizoguchi, T.; Nomura, K.; Ohta, S.; Nomura, T.; Nakanishi, Y.; Ikuhara, Y.; Hirano, M. Giant thermoelectric Seebeck coefficient of a two-dimensional electron gas in SrTiO3. *Nature materials* **2007,** *6* (2), 129.

(31) Ohta, H.; Mizuno, T.; Zheng, S.; Kato, T.; Ikuhara, Y.; Abe, K.; Kumomi, H.; Nomura, K.; Hosono, H. Unusually large enhancement of thermopower in an electric field induced two−dimensional electron gas. *Advanced materials* **2012,** *24* (6), 740-744.

(32) Hu, L.; Zhu, T.; Liu, X.; Zhao, X. Point defect engineering of high−performance Bismuth−Telluride−Based thermoelectric materials. *Advanced Functional Materials* **2014,** *24* (33), 5211-5218.

(33) Banik, A.; Vishal, B.; Perumal, S.; Datta, R.; Biswas, K. The origin of low thermal conductivity in $Sn_{1-x}Sb_xTe$: phonon scattering via layered intergrowth nanostructures. *Energy & Environmental Science* **2016,** *9* (6), 2011-2019.

Figure Caption

Figure 1. Powder XRD patterns of (a) $Ca_{0.9}Dy_{0.1}MnO_3$ and (b) $Ca_{0.9}Yb_{0.1}MnO_3$

Figure 2. (a) Electric resistivity (b) Seebeck coefficient (c) power factor and (d) total thermal conductivity (closed symbols) and lattice thermal conductivity (open symbols) as a function of temperature for multi-calcined $Ca_{0.9}Dy_{0.1}MnO_3$

Figure 3. Temperature dependence of (a) electrical resistivity (b) Seebeck coefficient (c) power factor and (d) total thermal conductivity (closed symbols) and lattice thermal conductivity (open symbols) for multi-calcined $Ca_{0.9}Yb_{0.1}MnO_3$

Figure 4. The figure of merit (zT) as a function of temperature for multi calcined (a) $Ca_{0.9}Dy_{0.1}MnO_3$ and (b) $Ca_{0.9}Yb_{0.1}MnO_3$

Figure 5. (a) maximum zT values vs calcination times and (b) percentage variation of power factor (PF), thermal conductivities (κ) and zT at 672 K normalized to CMO: R-1 (R=Dy, Yb)

Figure 6. SEM images of representative surface sections of (a) CMO: Dy-1 (b) CMO: Dy-3 (c) CMO: Yb-1 and (d) CMO: Yb-3

Figure 7. EDS elemental mapping for Mn (cyan), Ca (yellow), Yb (green) in composition of CMO: Yb-1 (left) and CMO:Yb-3 (right)

Figure 8 Transmission electron microscopy of CMO:Yb. (a) A low-magnification TEM image of samples CMO:Yb-3. (b) A medium-magnification TEM image of samples CMO:Yb-3. (c) HRTEM image of CMO:Yb-3. (d) HRTEM image of CMO:Yb-1.

Figure 9. Room temperature (a) carrier concentration (b) carrier mobility for $Ca_{0.9}R_{0.1}MnO_3$ (R= Dy, Yb)

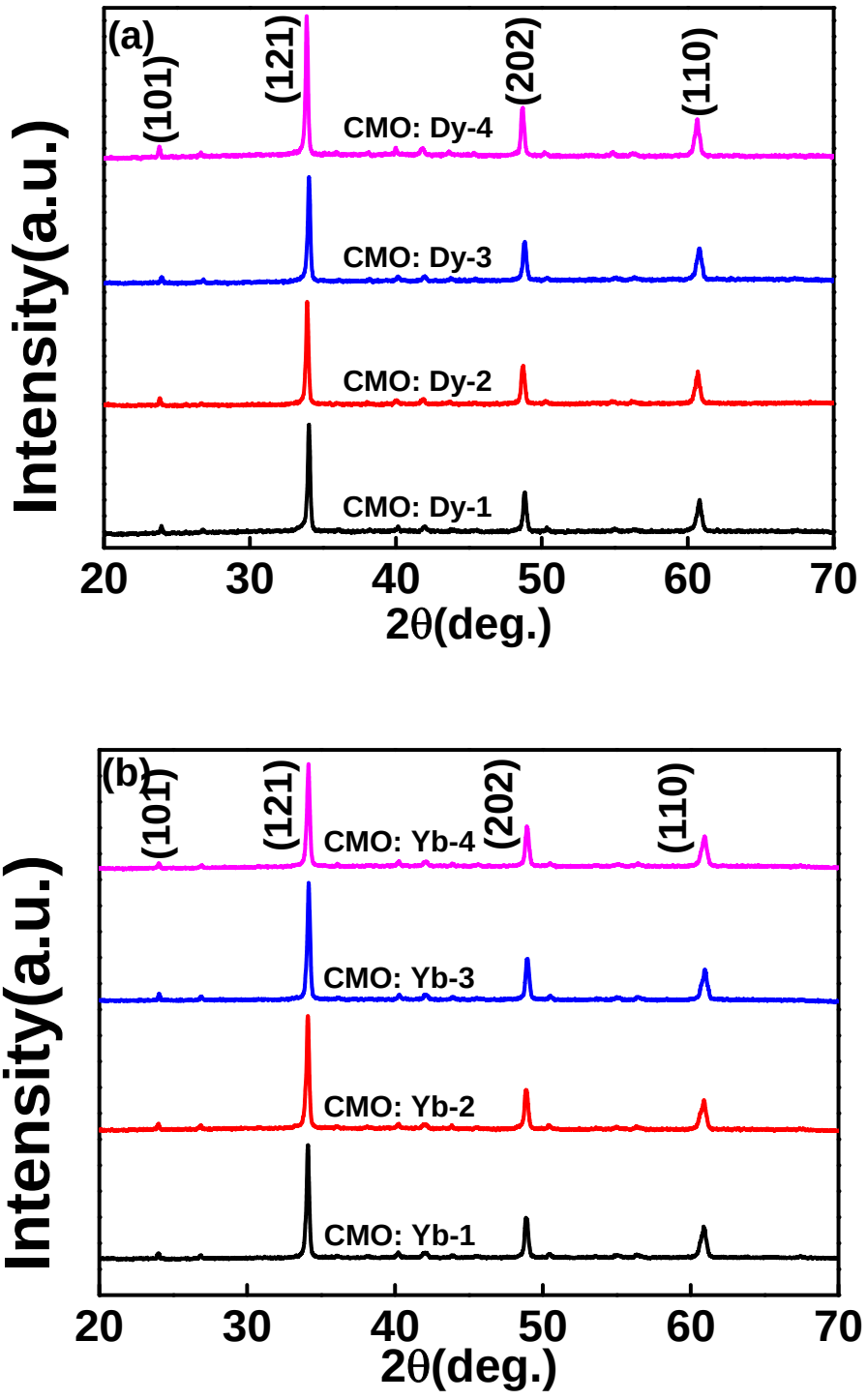

Figure 1. Powder XRD patterns of (a) $Ca_{0.9}Dy_{0.1}MnO_3$ and (b) $Ca_{0.9}Yb_{0.1}MnO_3$

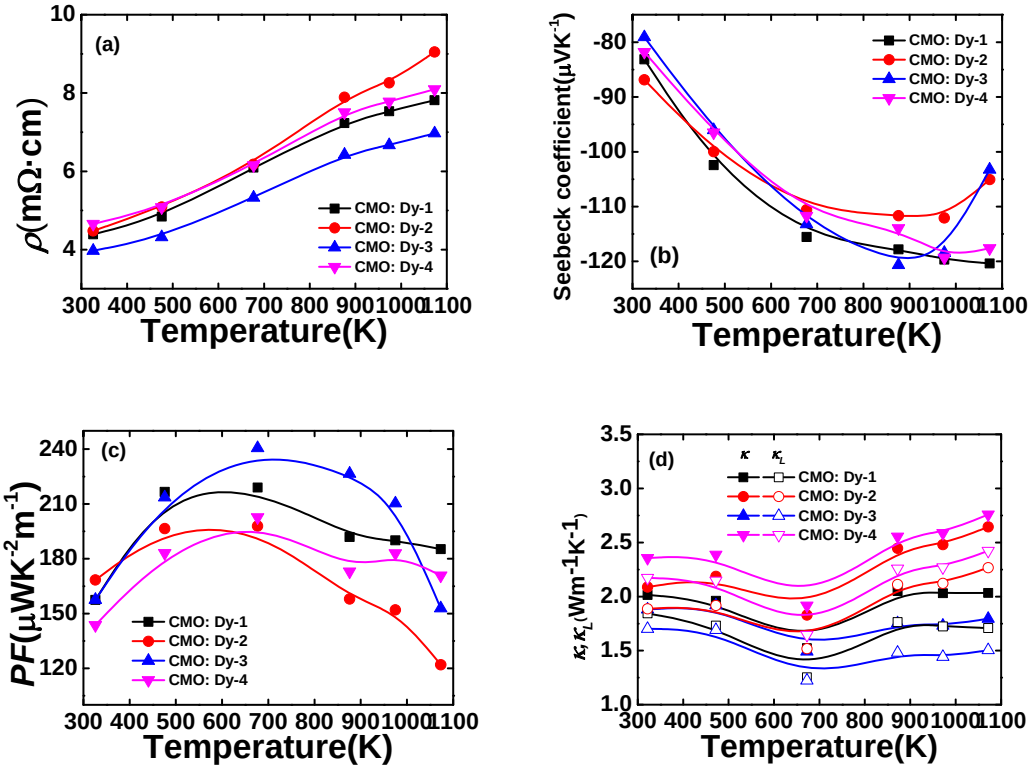

Figure 2. (a) Electric resistivity (b) Seebeck coefficient (c) power factor and (d) total thermal conductivity (closed symbols) and lattice thermal conductivity (open symbols) as a function of temperature for multi-calcined $Ca_{0.9}Dy_{0.1}MnO_3$

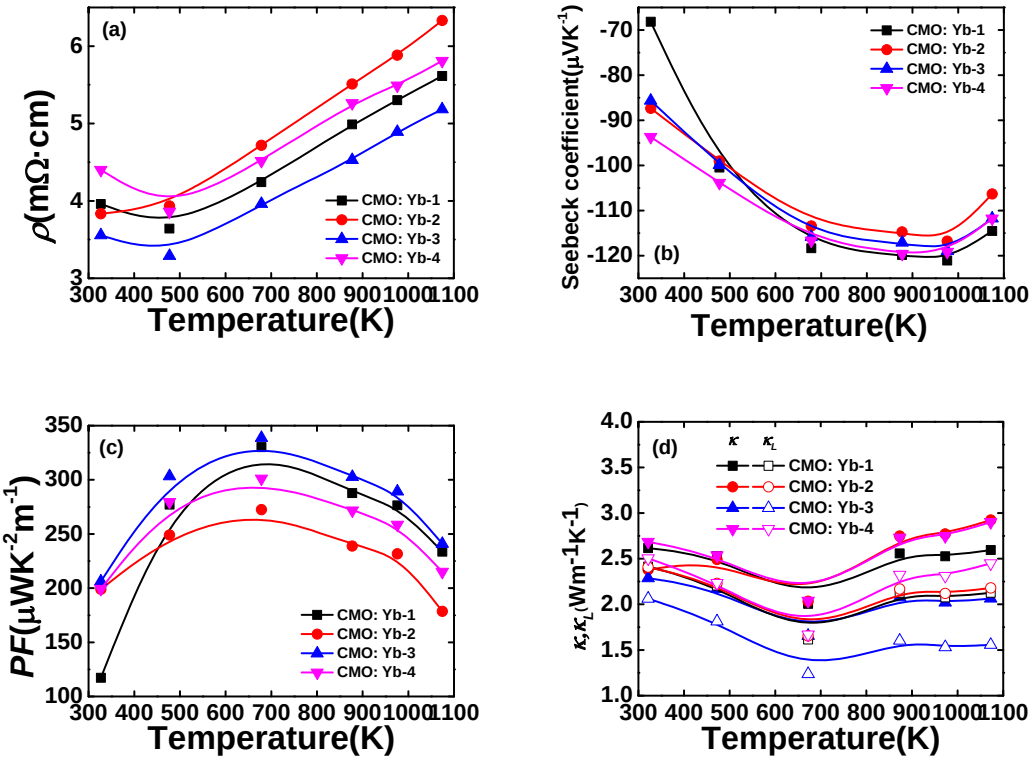

Figure 3. Temperature dependence of (a) electrical resistivity (b) Seebeck coefficient (c) power factor and (d) total thermal conductivity (closed symbols) and lattice thermal conductivity (open symbols) for multi-calcined $Ca_{0.9}Yb_{0.1}MnO_3$

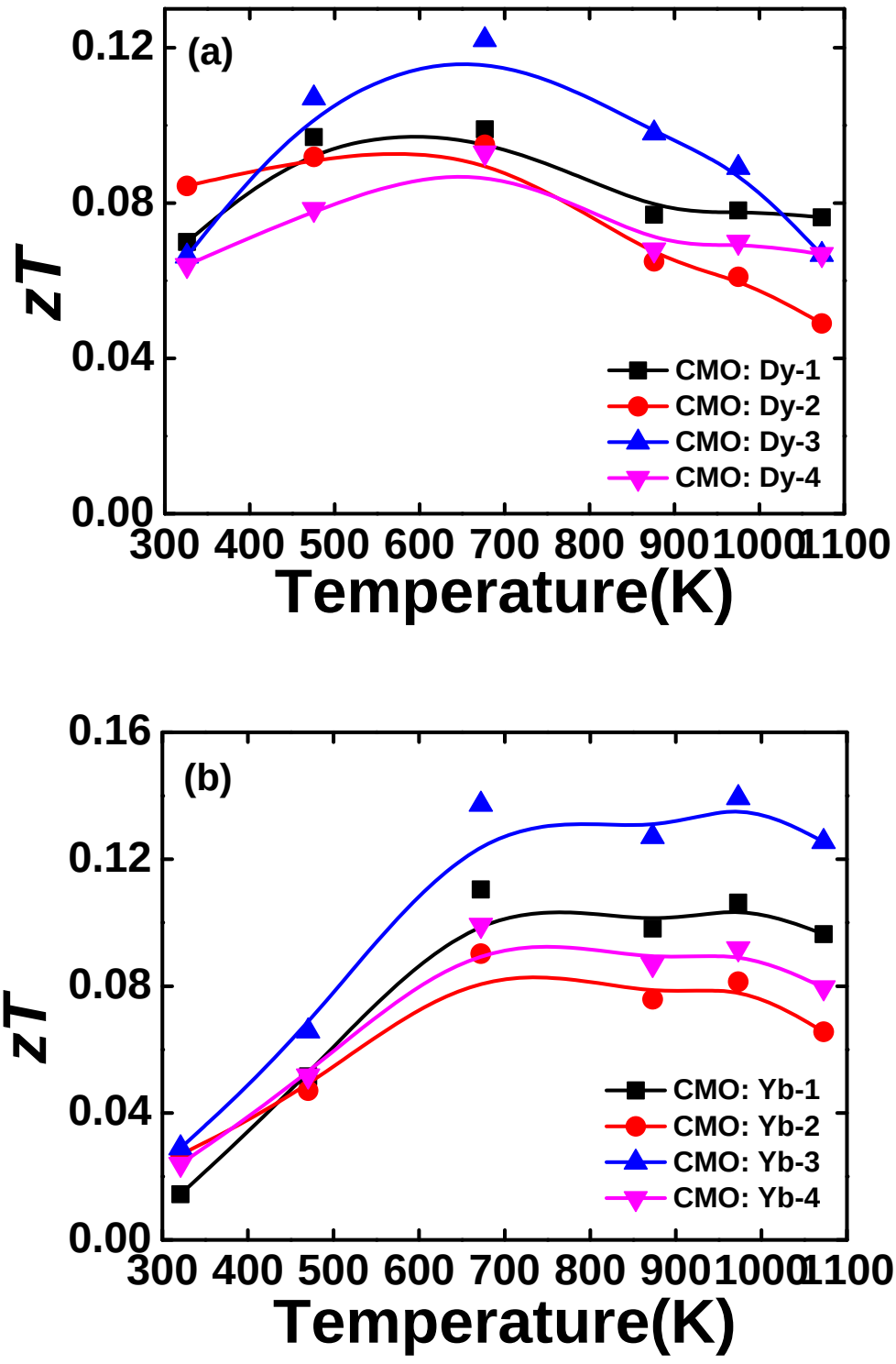

Figure 4. The figure of merit (zT) as a function of temperature for multi calcined (a) $Ca_{0.9}Dy_{0.1}MnO_3$ and (b) $Ca_{0.9}Yb_{0.1}MnO_3$

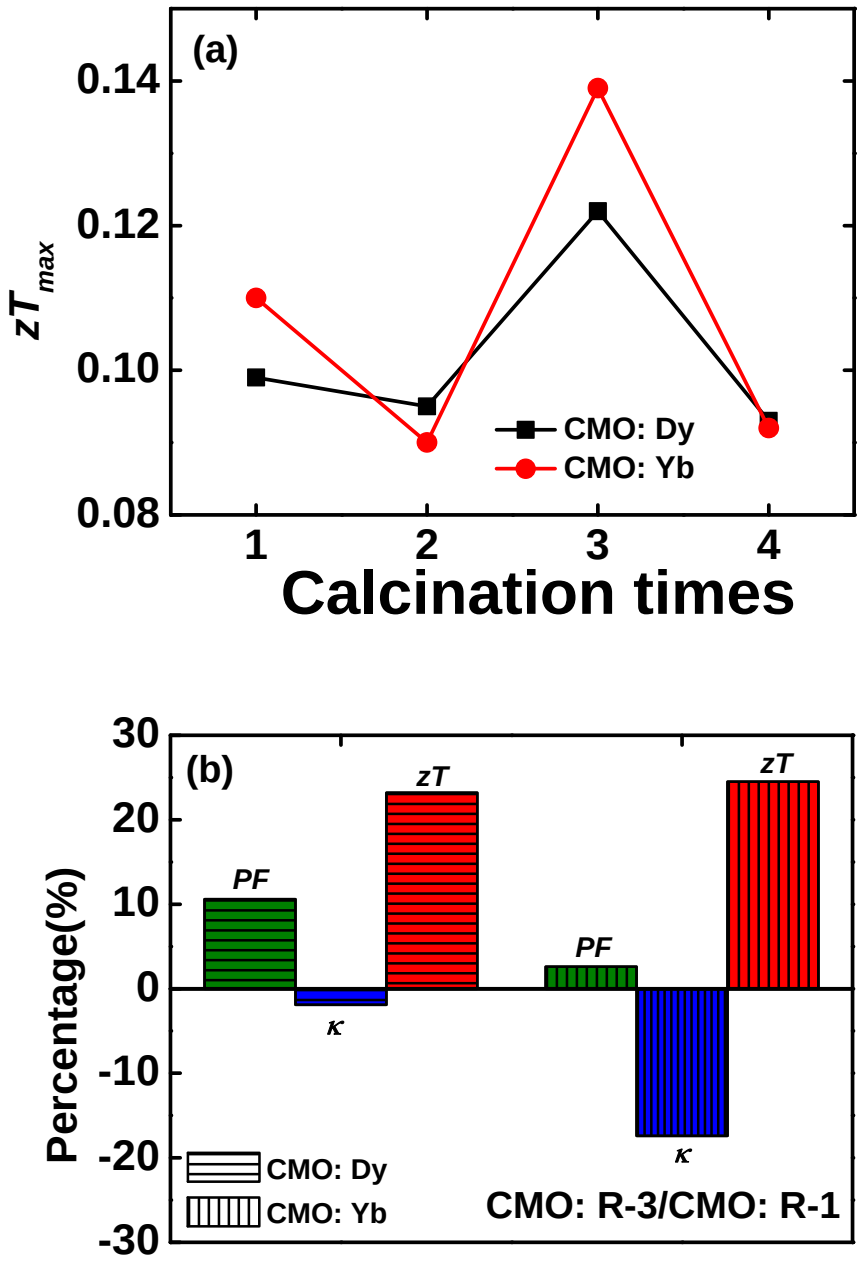

Figure 5. (a) maximum *zT* values vs calcination times and (b) percentage variation of power factor (*PF*), thermal conductivities (κ) and *zT* at 672 K normalized to CMO: R-1 (R=Dy, Yb)

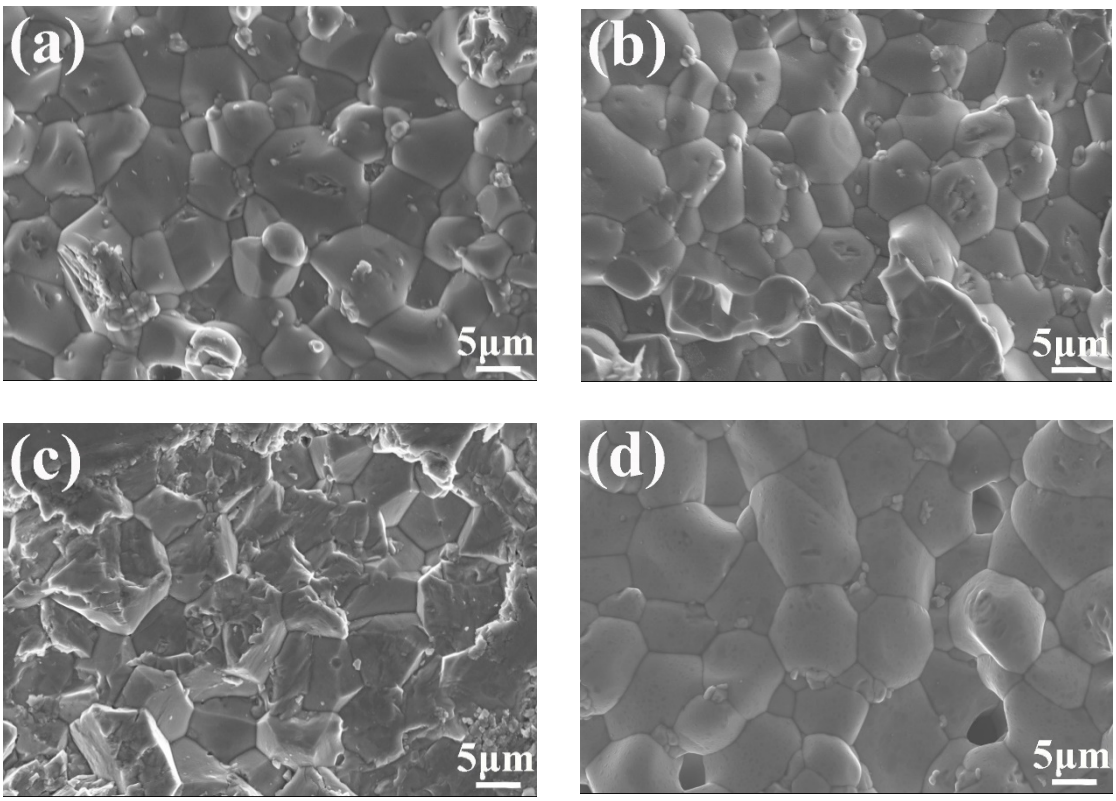

Figure 6. SEM images of representative surface sections of (a) CMO: Dy-1 (b) CMO: Dy-3 (c) CMO: Yb-1 and (d) CMO: Yb-3

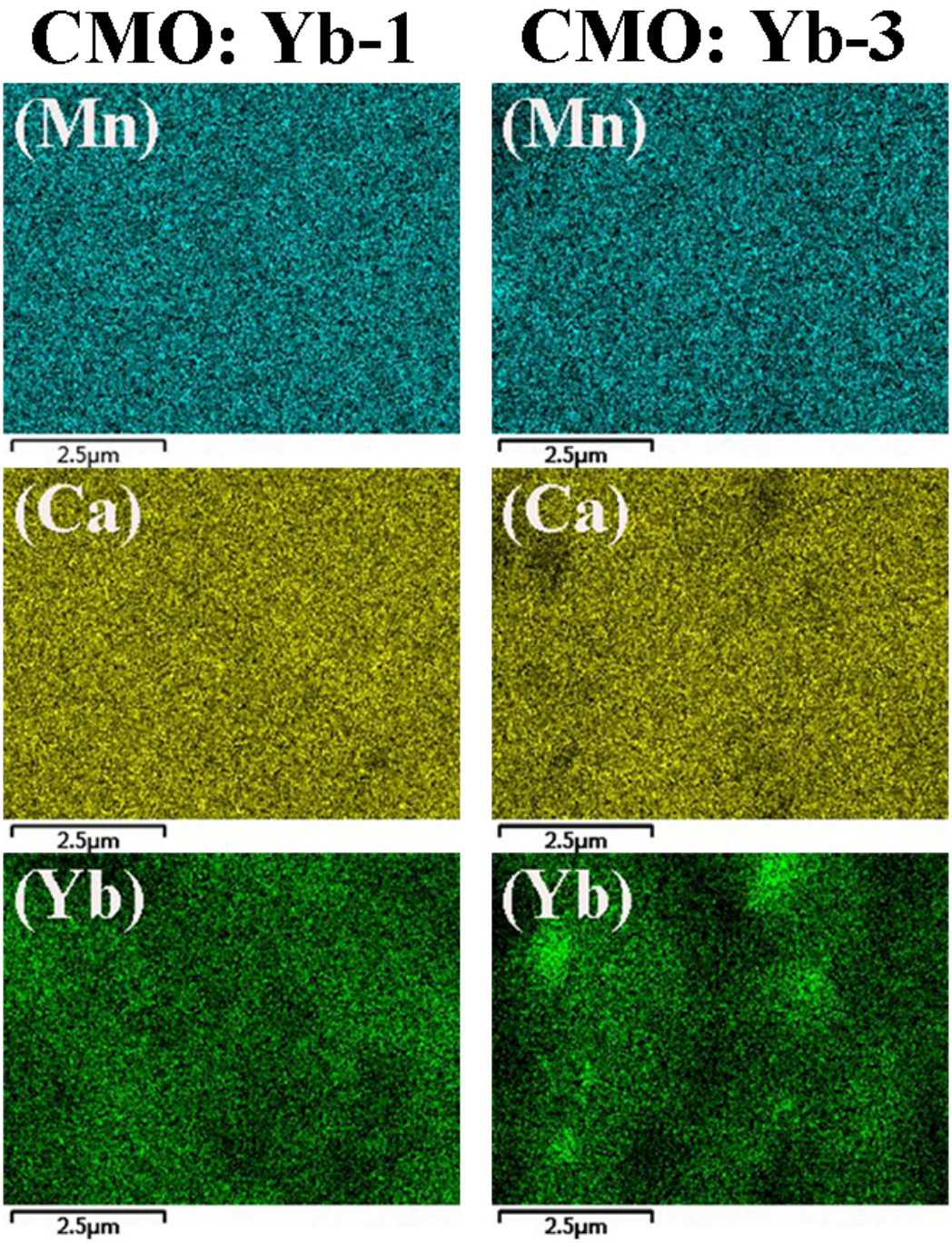

Figure 7. EDS elemental mapping for Mn (cyan), Ca (yellow), Yb (green) in composition of CMO: Yb-1 (left) and CMO: Yb-3 (right)

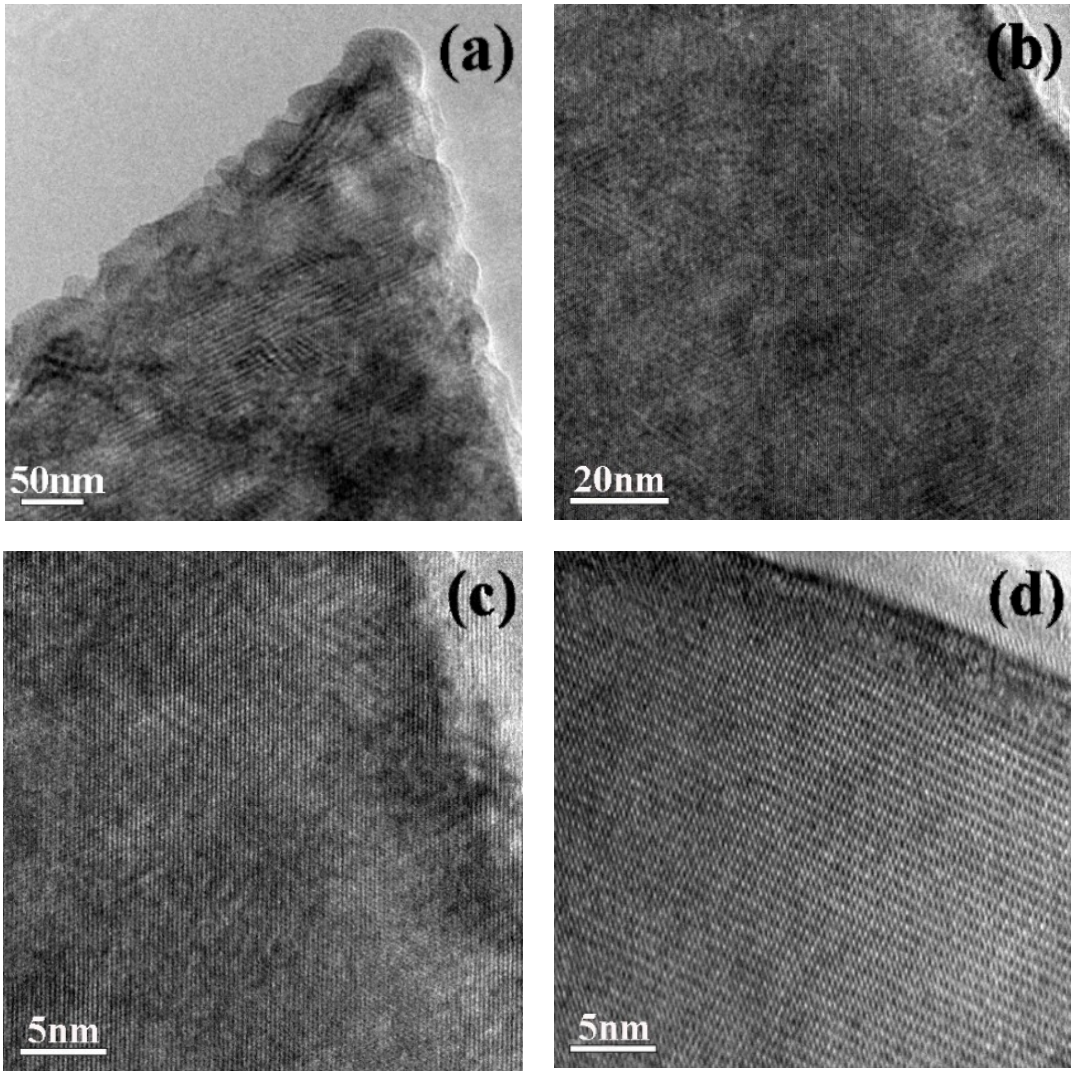

Figure 8 Transmission electron microscopy of CMO:–Yb. (a) A low-magnification TEM image of samples CMO:–Yb-3. (b) A medium-magnification TEM image of samples CMO:-Yb-3. (c) HRTEM image of CMO:-Yb-3. (d) HRTEM image of CMO: Yb-1.

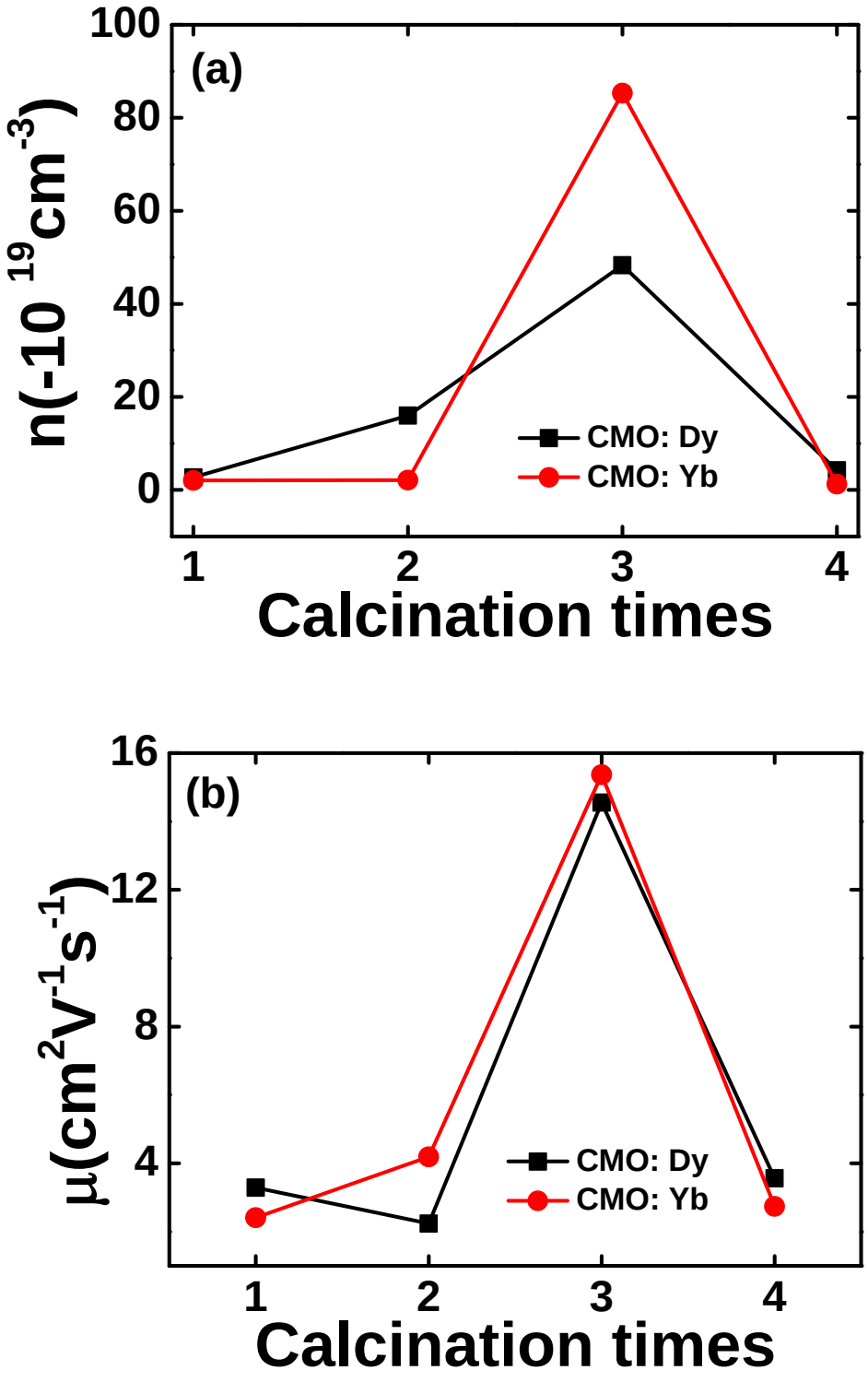

Figure 9. Room temperature (a) carrier concentration (b) carrier mobility for $Ca_{0.9}R_{0.1}MnO_3$ (R= Dy, Yb)